

Supporting Information

Chiral Polarized Photonic Chips *via* Organic Crystal Heterojunctions

Ya-Cheng Li¹, Hui-Ying Liu^{1}, Rui-Lin Yang², Fan Li¹, Xiao-Ning Wang¹, Xiao-Bin Chen¹, Xiu-Qi Chen²,
Hongbing Fu³, Chun-Lin Sun^{2*}*

1. School of Materials Design and Engineering, Beijing Institute of Fashion Technology, Beijing 100029(P. R. China)
2. State Key Laboratory of Applied Organic Chemistry (SKLAOC), Key Laboratory of Special Function Materials and Structure Design (MOE), College of Chemistry and Chemical Engineering, Lanzhou University, Lanzhou, 730000 (P. R. China)
3. Beijing Key Laboratory for Optical Materials and Photonic Devices, Department of Chemistry, Capital Normal University, Beijing, 100048 (P. R. China)

Table of contents

1. **Materials and experimental details**
2. **The absorption, the emission and time-resolved fluorescence spectra of pMSB and BPEA**
3. **Transient absorption spectra.**
4. **The SEM images and fluorescence microscopy (FM) images of branched heterostructures**
5. **The tunable morphologies of branches and trunks**
6. **The X-ray diffraction of BPEA microrods and pMSB hexagonal microsheets**
7. **The packing in crystal of pMSB and BPEA**
8. **The transition dipole moment of pMSB and BPEA**
9. **The natural transition orbitals (NTOs) for BPEA and pMSB**
10. **Home-built micro-photoluminescence (μ -PL) setup**
11. **Finite-difference time-domain (FDTD) simulation.**
12. **Reference**

1. Materials and experimental details

All the reagents and materials were purchased from J&K Chemical Co. (China), and are of analytical grade. The solvents were used as received without further purification.

The microcrystal morphologies were characterized by field-emission scanning electron microscopy (SEM, JEOL JSM-7500F) under an accelerating voltage of 5 kV. The microcrystals casted on copper grid were observed on a JEOL JEM 2100 transmission electron microscope with an accelerating voltage of 100 kV. The fluorescence images were taken by fluorescence microscopy Olympus BX 53 with Xenon lamp (330-380 nm for UV light). The X-ray diffraction measurements were made on a Bruker Discover D8 diffractometer with Cu-K α radiation ($\lambda = 1.54050 \text{ \AA}$) in the 2θ operated range from 3° to 50° .

2. The absorption, emission spectra and time-resolved fluorescence spectra of pMSB and BPEA

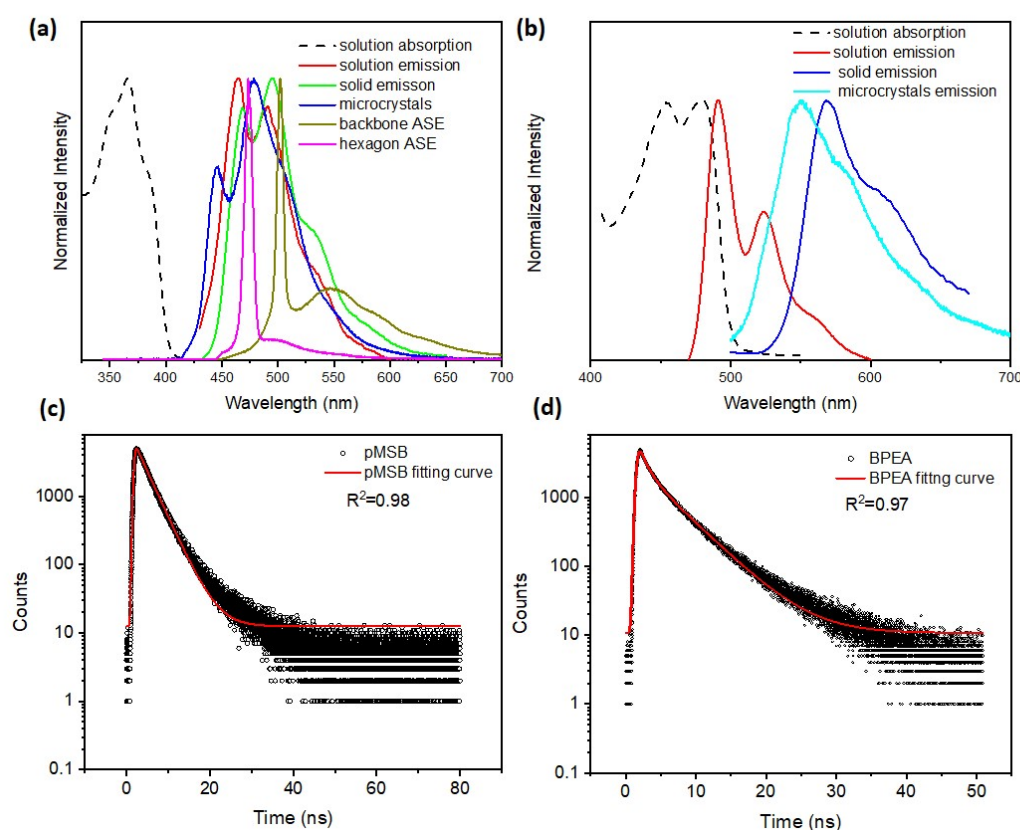


Figure S1. the absorption and emission spectra of (a) pMSB and (b) BPEA; the time-resolved fluorescence spectra of (c) pMSB and (d) BPEA.

Table S1. Spectroscopic parameters of the pMSB and BPEA.

	$\lambda_{\text{abs,sol}}$	$\lambda_{\text{em,sol}}$	$\lambda_{\text{em,solid}}$	$\lambda_{\text{em,crystal}}$	Φ	τ/ns	k_r/ns^{-1}	k_{nr}/ns^{-1}
pMSB	350,365,389	463,490,537	467,495,533	445,480,502	0.89	3.1	0.29	0.035
BPEA	440, 466	490,523,560	567,606	550,583	0.18	2.4	0.075	0.29

$\lambda_{\text{em}}(\text{nm})$ is the energy of the peak of the fluorescence band; Φ is the fluorescence quantum yields; τ (ns) is the lifetime of fluorescence; The last two columns provide the rate constant for radiative deactivation S_1 to S_0 , k_r (ns^{-1}) and the rate constant for non-radiative deactivation, k_{nr} (ns^{-1}).

3. Transient absorption spectra

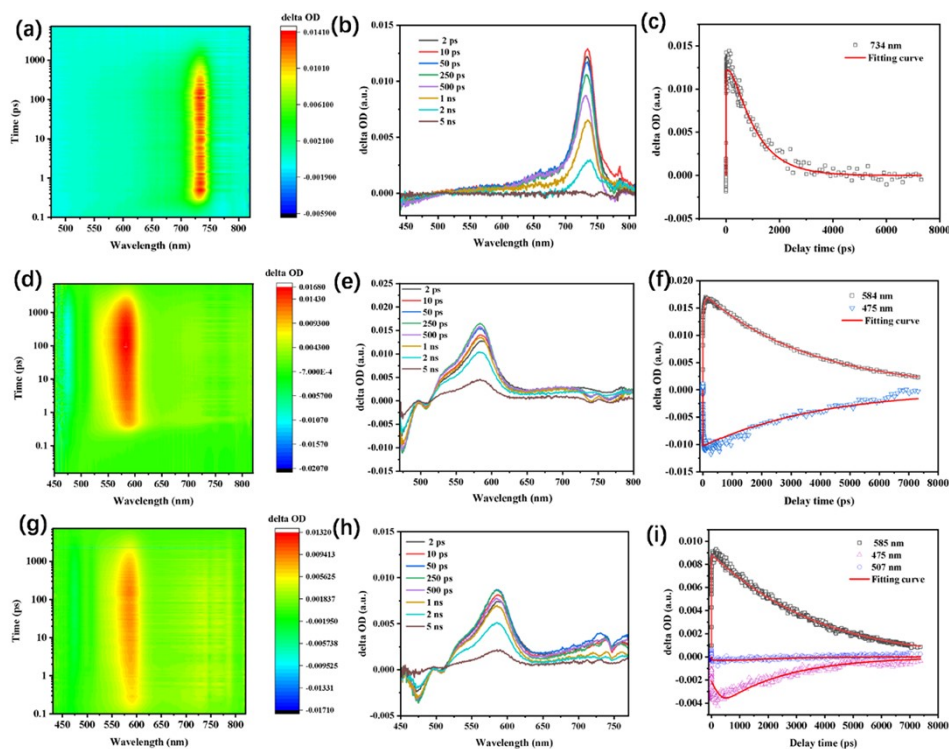


Figure S2. The femtosecond transient absorption (fs TA) kinetics decay curve fitting for pMSB, BPEA and pMSB-BPEA nanoparticle suspension in ethanol and cyclohexane mixed solvent.

Table S2. The kinetics decay curves and their fitting data at representative wavelength

pMSB NPs			BPEA NPs				BPEA-pMSB NPs			
λ	τ_l	τ_2	λ	τ_l	τ_2	τ_3	λ	τ_l	τ_2	τ_3
734	98.9 (-0.167)	1060 (0.833)	475	3850 (-0.0048)	-	-	475	2340	-	-
-	-	-	584	3270 (0.762)	-	-	507	1040	-	-
-	-	-	-	-	-	-	584	50.6 (-0.120)	3170 (0.438)	2600 (0.442)

The λ presents the representative wavelength (nm). The lifetimes (τ) are in ps, and the values in parentheses indicate the relative amplitude (A) of each decay component obtained from multi-exponential fitting. “-” denotes absence of a component.

4. The SEM images and fluorescence microscopy (FM) images of branched heterostructures

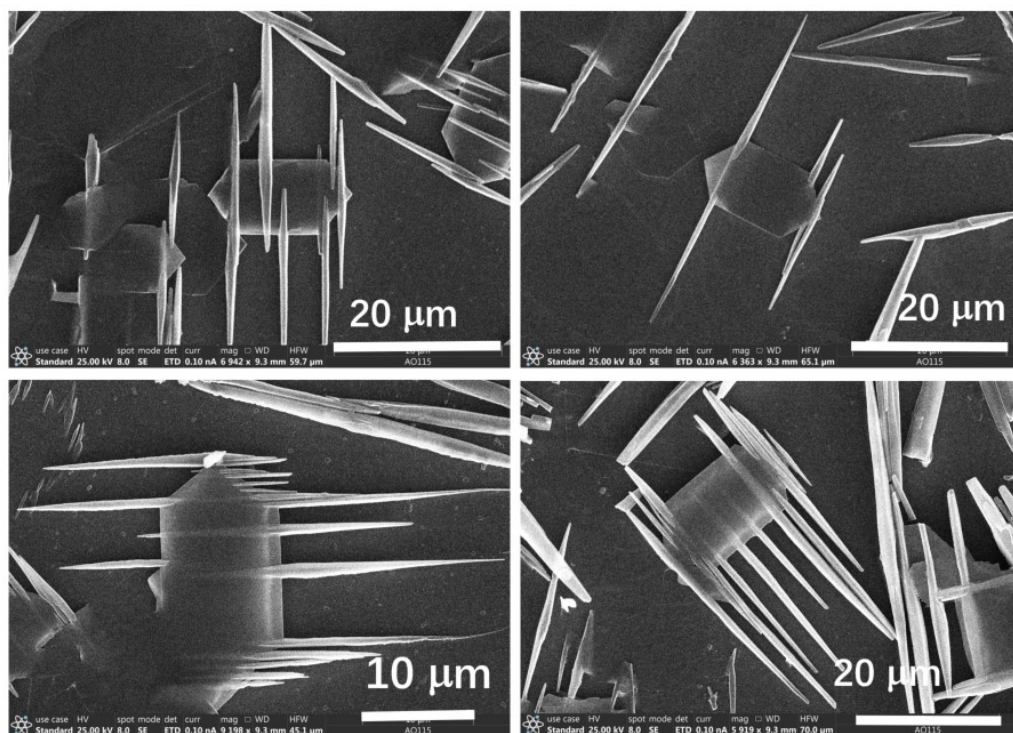


Figure S3. Scanning electron microscopy (SEM) images of branched heterostructures, scale bars are indicated in the images.

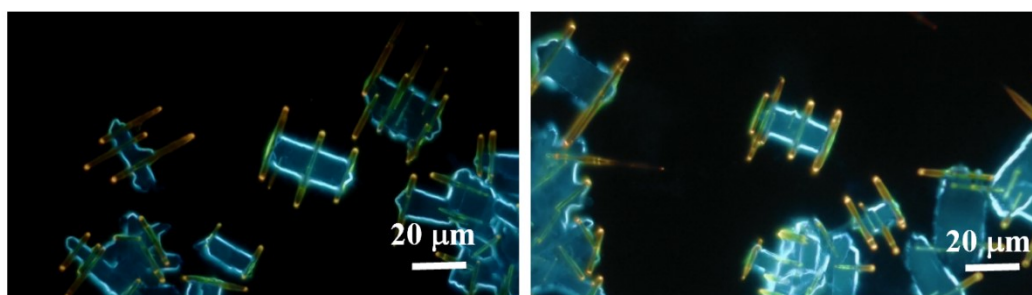


Figure S4. Fluorescence microscopy (FM) images of branched heterostructures, scale bars are indicated in the images.

5. The tunable morphologies of branches and trunks

A dichloromethane solution of BPEA with a concentration of 5 mM was prepared, along with a series of poor solvents with varying ratios of cyclohexane to anhydrous ethanol. A 200 μL aliquot of the mother liquor was injected into each of the poor solvents, allowed to stand for 5 minutes, and then a sample was dropped onto a glass slide. After the solution had evaporated, BPEA crystals were obtained. It is noteworthy that as the proportion of anhydrous ethanol in the poor solvent increased, the BPEA crystals gradually transformed from one-dimensional curved linear crystals with orange luminescence to one-dimensional rod-like crystals with orange-yellow luminescence, in Figure S5.

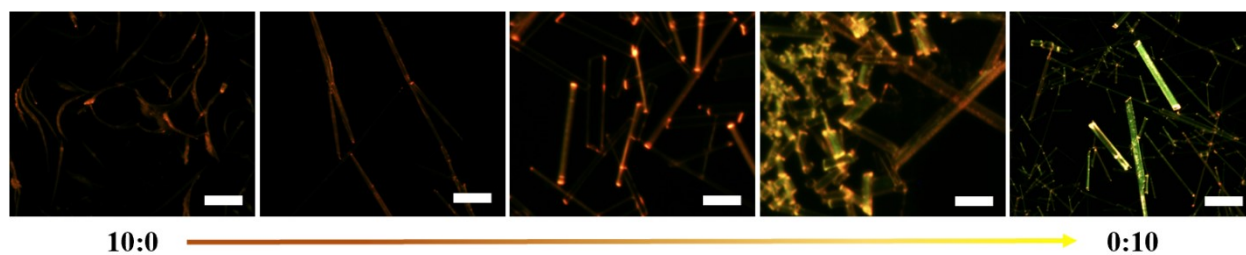


Figure S5. Fluorescence microscopy (FM) images of BPEA crystals with varying cyclohexane to ethanol ratios (10:0 to 0:10), scale bar: 10 μm .

The assembly of pMSB solute molecules saturated in dichloromethane is strongly influenced by poor solvents, as shown in Figure S6. In pure cyclohexane, crystals form curved 1D needle-like curved structures. Increasing the anhydrous ethanol ratio in the poor solvent results in straighter and shorter 1D microwires, while pure anhydrous ethanol yields 2D elongated hexagonal crystals. Thus, tuning the poor solvent composition enables precise control over pMSB crystal morphology, from 1D to 2D structures.

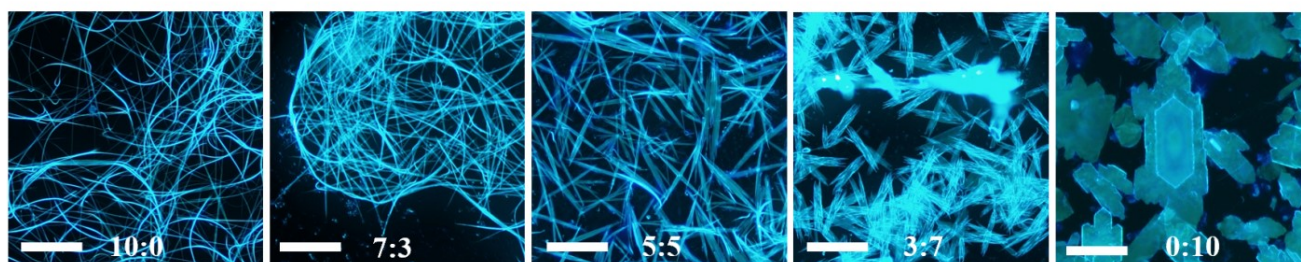


Figure S6. Crystal morphologies of pMSB after re-precipitation with varying cyclohexane to ethanol ratios (10:0 to 0:10), scale bar: 10 μm .

Upon solvent exchange from CS_2 to dichloromethane (DCM) in pMSB saturated solutions, evaporation yielded two distinct hexagonal microsheet morphologies: regular hexagons and elongated hexagons. Aspect ratio analysis revealed $R_{\text{CS}_2} = 0.35$ versus $R_{\text{DCM}} = 0.94$ (where $R = l_s/l_l$, representing short-to-long side ratio; see Figure S7, upper right). This marked difference suggests solvent-dependent anisotropic growth modulation, where CS_2 and DCM differentially inhibit/promote specific crystal faces ([200] and [020] directions). Three potential mechanisms emerge: (1) preferential [200] stacking promotion, (2) [020] stacking inhibition, or (3) synergistic combination of both effects (Figure S7c).

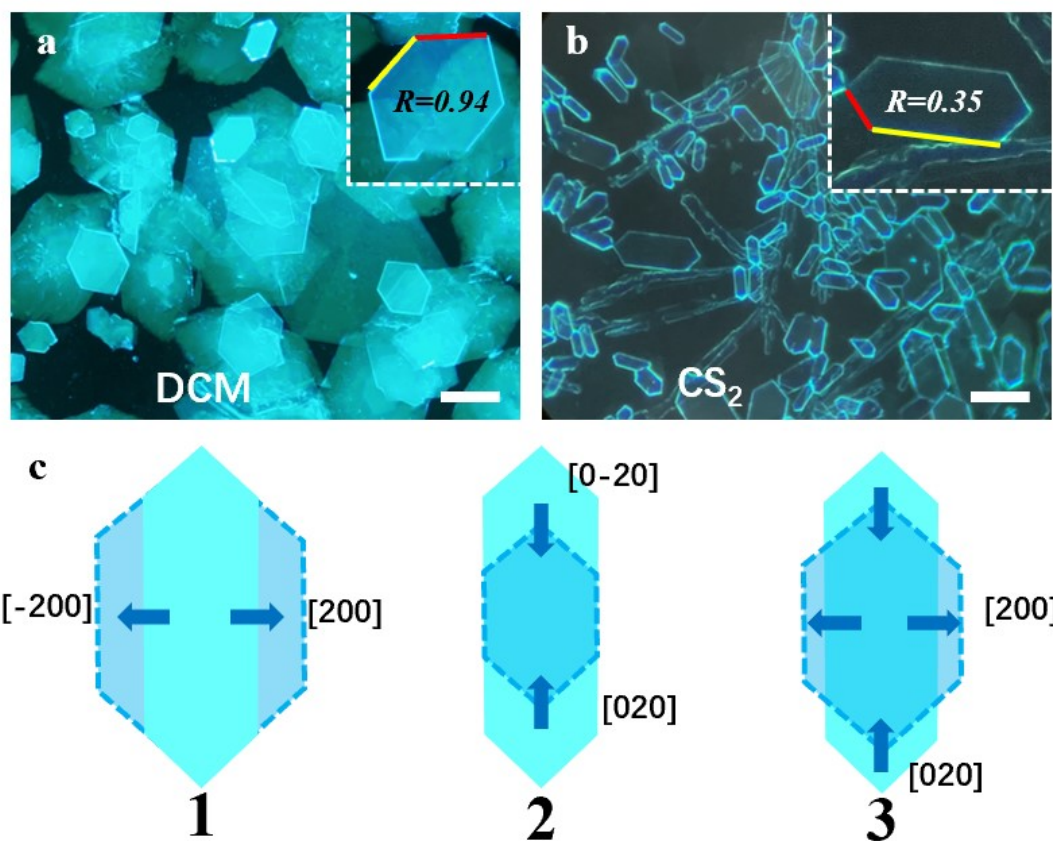


Figure S7. Crystal morphologies of pMSB after (a) DCM evaporation and (b) CS_2 evaporation (c) the illustration of growth direction of hexagons of pMSB. Scale bar: 10 μm .

6. The X-ray diffraction of microcrystals of BPEA and pMSB

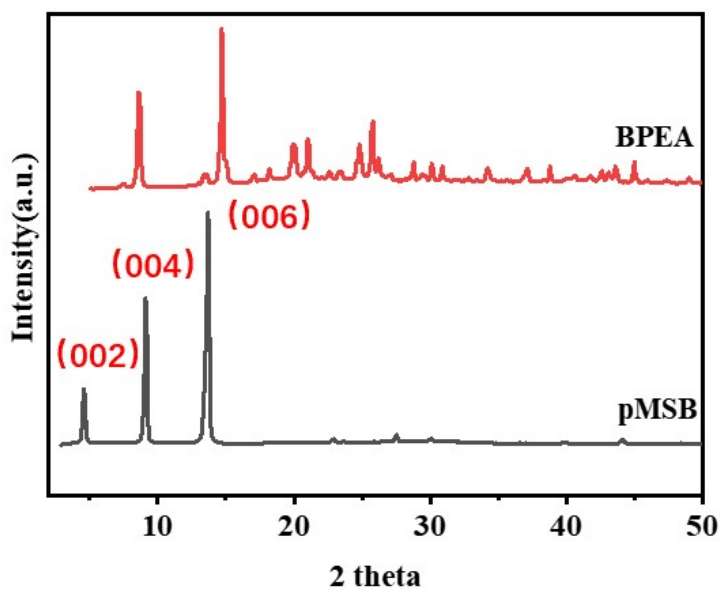


Figure S8. The X-ray powder diffraction of BPEA microrods and pMSB hexagonal microsheets.

7. The packing in crystal of pMSB and BPEA.

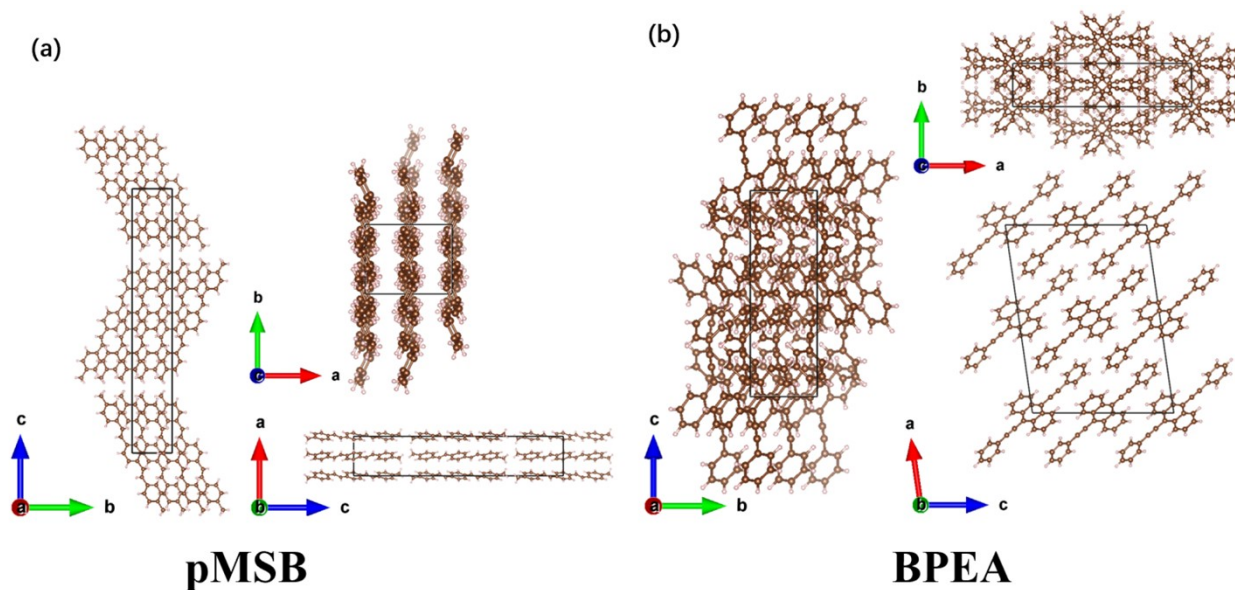


Figure S9. Crystal packing of pMSB viewed through the bc plane, ab plane and ac plane; Crystal packing of BPEA viewed through the bc plane, ab plane and ac plane; X-ray crystallographic data can be obtained free of charge from the Cambridge Crystallographic Data Center (www.ccdc.cam.ac.uk/data_request/cif) under accession numbers CCDC: 708328^{S1} and 855467^{S2}.

8. The transition dipole moment of pMSB and BPEA

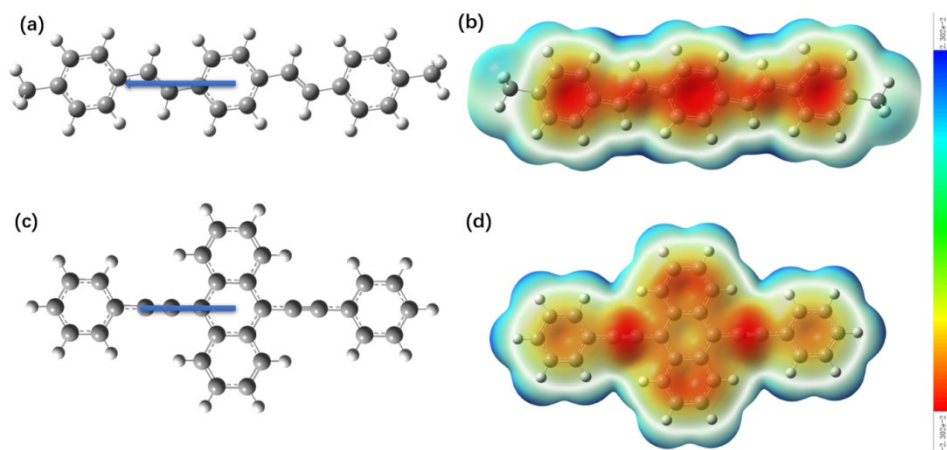


Figure S10. The transition dipole moment of pMSB and BPEA.

9. The natural transition orbitals (NTOs) for BPEA and pMSB.

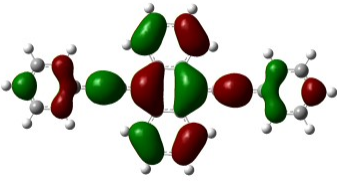
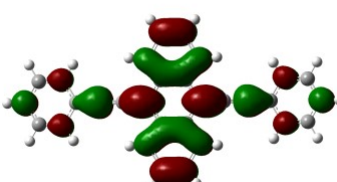
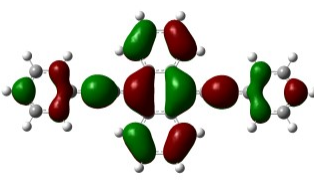
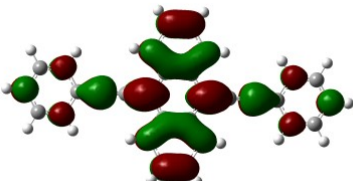
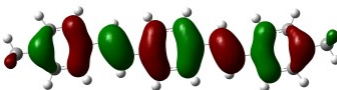
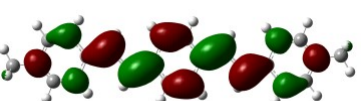
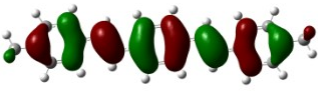
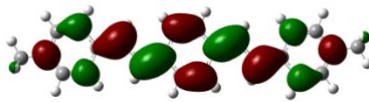
Molecules		Hole	Particle
BPEA	$ 1\rangle_A$ $W=0.99611$ $f=0.8016$ 2.3837 eV		
	$ 1^*\rangle_A$ $W=1.0000$ $f=0.7732$ 2.1291 eV		
pMSB	$ 1\rangle_A$ $W=0.99625$ $f=1.8782$ 3.0002 eV		
	$ 1^*\rangle_A$ $W=1.0000$ $f=1.9943$ 2.6471 eV		

Figure S11. Natural transition orbitals describing the first and second optimized ground states (absorption), the lowest optimized excited state (emission) bright states. The numbers in the left column indicate the corresponding excited-state number, fraction of the NTO pair contribution into the given electronic excitation, w ; the excitation energy in eV; and f , the oscillator strength for the one-photon-absorption (OPA) excitations.

10. Schematic illustration of the home-built μ -PL system

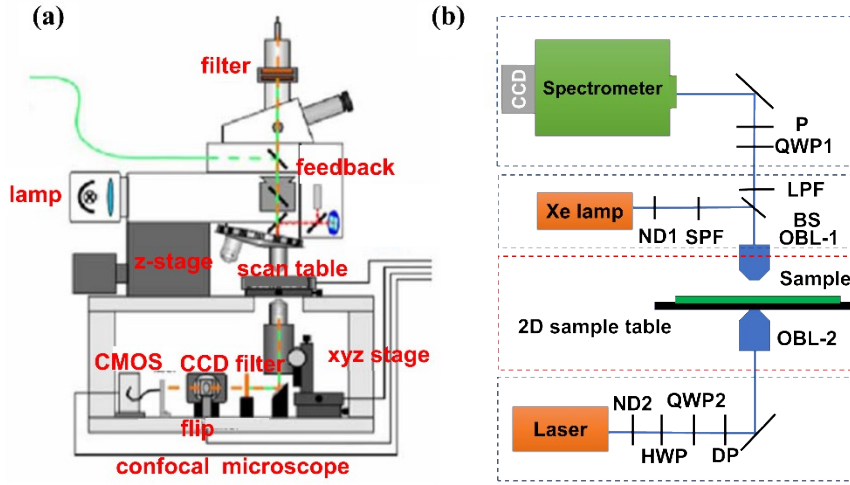


Figure S12. Schematic illustration of the home-built μ -PL system (a) the modified confocal laser scanning microscope, and (b) the optical path for the waveguide measurements and CPL measurements.

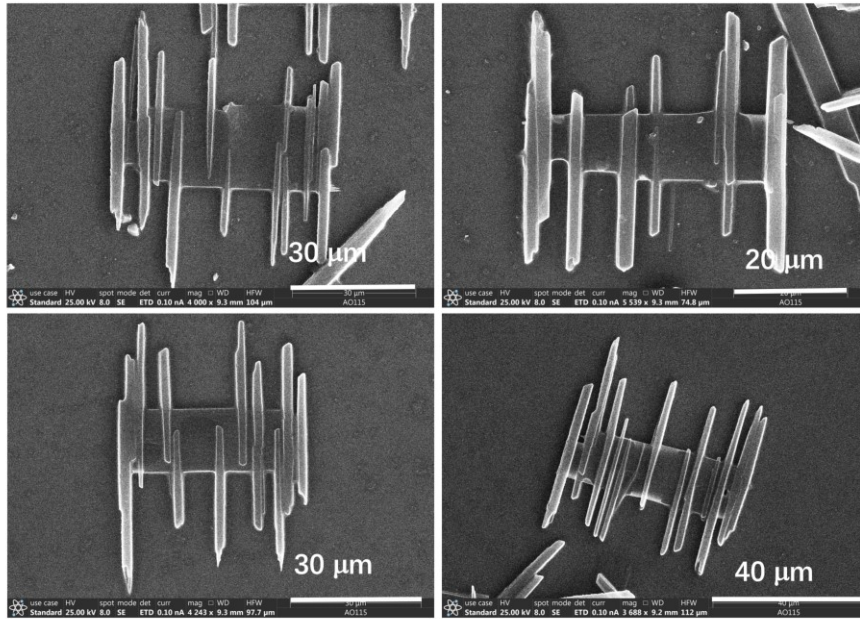


Figure S13. The SEM of typical morphologies of branched heterostructures, Scale bars are labeled.

11. Finite-difference time-domain (FDTD) simulation.

The quality factor (Q) of a micro-crystal resonator was calculated using the Finite-Difference Time-Domain (FDTD) method with a simplified planar structure. Based on the size and morphology of the micro-crystal, a 2D dielectric resonator was employed as a simplified computational model. A broadband optical field, centered at the emission wavelength, was used to excite cavity modes and obtain the optimal resonant eigenfrequency. The corresponding quality factor was calculated using

the formula $Q=\omega_0/\Delta\omega$ where: ω_0 is the resonant angular frequency, corresponding to the central frequency of the resonance peak and represents the natural frequency at which the system oscillates most efficiently and $\Delta\omega$ is the full width at half maximum (FWHM) of the resonance peak.

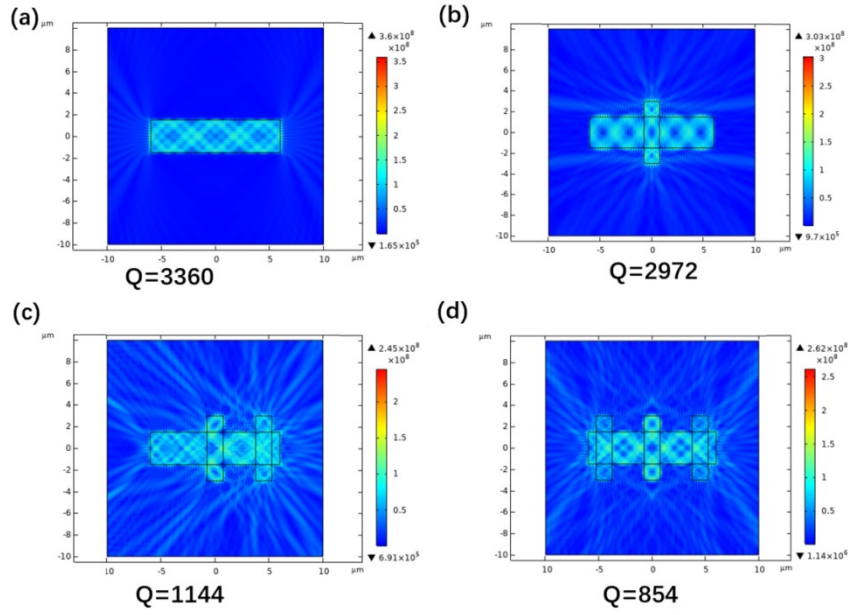


Figure S14. Electric field distribution from finite element calculations, (a) the main chain without branches, (b) heterojunction with one branch, (c) heterojunction with two branches and (d) heterojunction with three branches.

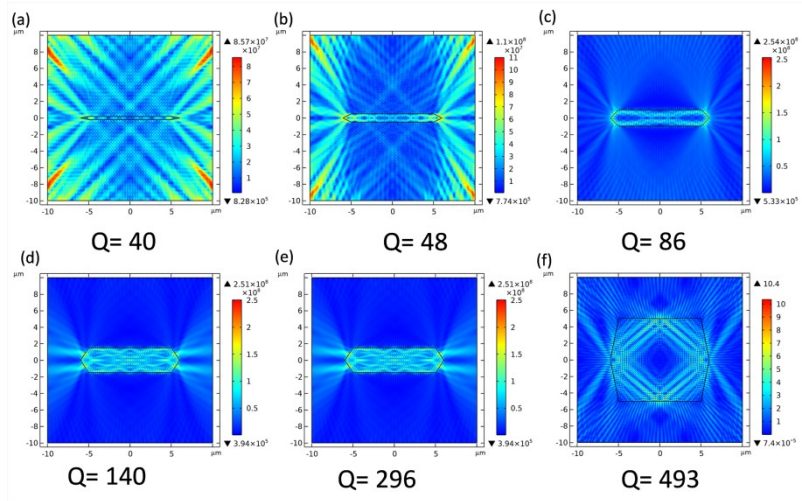


Figure S15. Electric field distribution from finite element calculations of the elongated-hexagonal trunk of heterojunction with increasing width: (a) 0.1 μm , (b) 0.5 μm , (c) 1 μm , (d) 1.5 μm , (e) 2.5 μm , and (f) 5 μm .

To quantitatively elucidate the relationship between crystal morphology and optical cavity performance, we conducted finite-difference time-domain (FDTD) simulations on heterostructures with a fixed length of 12 μm and widths varying from 0.1 to 5 μm . The simulations reveal a remarkable increase in the quality factor (Q) from 40 to 493 as the morphology transitions to a hexagonal form, thus confirming its optical advantages of hexagonal morphology

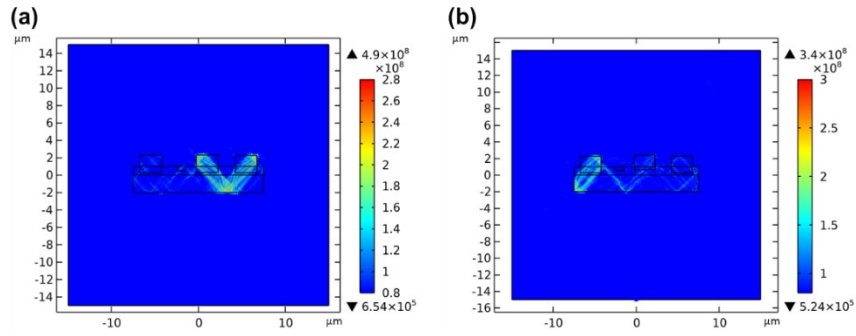


Figure S16 Electric field distribution from finite-difference time-domain (FDTD) simulations based on the heterojunction side view, incorporating the main chain, branches, overlapping layers, and defect sites. (a) continuity of waveguide modes among the three branches. (b) non-reversibility of waveguide phenomenon caused by a slight rotation of the middle branch.

12. Reference

[S1] R. Kabe, H. Nakanotani, T. Sakanoue, M. Yahiro, C. Adachi, *Adv. Mater.*, 2009, 21, 4034, DOI: 10.1002/adma.200803588

[S2] A. S. Batsanov, J. C. Collings, T. B. Marder (2013). Private communication (deposition number 855467). CCDC, Cambridge, England.